Identification and Prediction of Broadband Noise for a Small Quadcopter

Nicole A. Pettingill
Research Aerospace Engineer
Aeroacoustics Branch, NASA
Langley Research Center
Hampton, VA, U.S.A.

Nikolas S. Zawodny
Research Aerospace Engineer
Aeroacoustics Branch, NASA
Langley Research Center
Hampton, VA, U.S.A.

ABSTRACT

The growing interest in the noise of small unmanned aircraft systems (sUAS) in operation has motivated this study to characterize and predict broadband rotor noise sources. This paper analyzes the performance and acoustic data collected from two sets of wind tunnel experiments for hover and forward flight operating conditions. The first set of data is a result of testing a representative vehicle configuration of the Straight Up Imaging (SUI) Endurance quadcopter, while the second set of data represents an isolated rotor from the same vehicle. Following the analysis of the empirical data, a broadband noise prediction methodology is employed to compare with the experiments. This methodology uses NASA's ROTONET and BARC tools to predict blade loading and self-noise at conditions matching the wind tunnel experiments. This methodology is effective at predicting the broadband noise at certain conditions. Furthermore, some predictions are repeated with the inflow conditions calculated by the rotorcraft analysis tool CAMRAD II, which shows improved prediction results for cases with nonuniform inflow. This work confirms some of the unique challenges associated with testing small rotor configurations, explores the limitations of this prediction methodology, and suggests improvements that can be made for future studies.

NOMENCLATURE

$c_\circ$	Ambient speed of sound, (m/s)
D_f	Fuselage drag force, (N)
D_r	Rotor drag force, (N)
H	Radial segment trailing edge bluntness,(m)
L	Distance from rotor hub to vehicle CG, (m)
M	Blade element Mach number
M_∞	Wind tunnel freestream Mach number
r	Radial distance from hub, (m)
R	Rotor radius, (m)
T_r	Vehicle thrust or individual rotor thrust, (N)
$\mathbf{X}$	Global wind tunnel coordinate system, (X, Y, Z)
$\mathbf{x_v}$	Vehicle rotor plane coordinate system, (x_v, y_v, z_v)
V	Blade element local velocity, (m/s)
V_∞	Wind tunnel speed, (m/s)
α_v	Vehicle or rotor hub plane angle of attack, relative to the wind freestream velocity direction, (deg.)
α	Blade element effective local angle of attack, relative to the blade section, (deg.)
$\alpha_\circ$	Radial segment zero-lift angle of attack, (deg.)
β	Rotor blade twist, (deg.)
$\theta_\circ$	Wind tunnel observer angle to model test stand, (deg.)
θ	Source to observer microphone angle, (deg.)
θ_c	Shear layer corrected observer angle, (deg.)
μ	Advance ratio, $(V_\infty/\Omega R)$
ϕ	Rotor azimuth angle, (deg.)
ψ	Trailing edge angle, (deg.)
Ω	Main rotor rotational speed, (rad./s or RPM)

Presented at the Vertical Flight Society 75th Annual Forum & Technology Display, Philadelphia, Pennsylvania, May 13–16, 2019.

INTRODUCTION

Small unmanned aircraft systems, or sUAS, have experienced a recent increase in demand due to their advantages in size and maneuverability. With this demand comes concerns about the noise impact these vehicles will have on people in their vicinity. As sUAS technology develops, the need arises to characterize rotor noise and to develop tools that can reliably predict sUAS noise. The noise signatures of sUAS rotors differ from those of full-scale helicopter rotors due to their differences in size, tip speeds, performance requirements and other factors. These small rotors can have diameters that are 20-50 times smaller than those of traditional helicopter rotors, while also experiencing significantly lower tip speeds. For this reason, broadband noise may have a comparable amplitude to that of the blade passage frequency (BPF) and associated harmonics that tend to dominate conventional helicopter rotors. Additionally, multicopter configurations have multiple rotors that could aerodynamically interact with each other, resulting in more complex noise-generation mechanisms.

The possible interactions between rotors have inspired test campaigns like that of Tinney and Sirohi, who examined a series of performance and acoustic data to understand the noise

signatures of multicopters at hover thrust conditions (Ref. 1). However, fewer empirical results have been published for the broadband noise contributions present in these configurations, as well as interaction effects for forward flight conditions. A different test campaign of various multicopter configurations was conducted in the US Army 7- by 10-Foot Wind Tunnel at the NASA Ames Research Center in 2015 (Ref. 2). Acoustic contamination and lack of directivity measurements limited the acoustic data presented; however, the report provided a robust set of performance data, which Russell et al. supplemented and analyzed for two quadcopter configurations (Ref. 3). At NASA Ames, hover and forward flight computational modeling of the Straight Up Imaging (SUI) Endurance quadcopter predicted possible aerodynamic interactions between rotors (Ref. 4).

Airfoil self-noise, also known as trailing edge noise, has generated considerable interest in the aeroacoustics community due to it being a universal broadband noise source in turbomachinery, turbines, wings, and rotors. Trailing edge noise is always present in lifting surfaces, as it is generated by the airfoil itself and not external unsteady inflow mechanisms such as turbulence ingestion or blade wake interaction. This motivated research efforts into investigating self-noise in the 1970s and 80s. Some of these efforts focused on prediction methods and include Amiet's Ffowcs-Wiliams and Hawkings (FW-H) model based approach (Ref. 5) followed by a semiempirical self-noise prediction method developed by Brooks et al. (Ref. 6). This semiempirical prediction method was first rotor-implemented for a BO-105 helicopter rotor model test in the Duits-Nederlandse Windtunnel (DNW) (Ref. 7). This was followed by an improved rotorcraft application of the code by Brooks and Burley (Ref. 8). This broadband rotor noise prediction method became the Broadband Acoustic Rotor Codes (BARC) suite (Ref. 9). BARC has historically been applied to large scale rotors, but very recently its application to small rotors such as the APC-SF has proven promising (Ref. 10). All the aforementioned studies have contributed to the understanding of self-noise sources and the mechanisms that cause them, while motivating many recent studies to be conducted on this topic.

The present investigation aims to identify and characterize the broadband noise sources of small rotors using both experimental data sets and self-noise predictions. It describes the relative importance of broadband and periodic noise contributions for different rotor configurations and flight conditions. It also explores the correlations between thrust conditions and noise. NASA's Rotorcraft Noise Prediction System (ROTONET) (Ref. 11), the Comprehensive Analytical Model of Rotorcraft Aerodynamics and Dynamics (CAMRAD II) (Ref. 12) and the Broadband Acoustic Rotor Codes (BARC) are used to predict blade loading and self-noise generated by the blades.

This research contributes to a deeper understanding of:

1. The relative broadband and periodic noise contributions for different rotor configurations and flight conditions;
2. The correlations between performance conditions and broadband self-noise;
3. The self-noise mechanisms that could be present in small rotors;
4. The effectiveness of a low fidelity prediction approach for broadband noise to aid future prediction efforts for small-scale rotors in edgewise forward flight.

This paper will first provide a background on rotor noise sources associated with small-scale UAS. It will then describe the experimental setup and data processing methods utilized, and an analytical methodology description will introduce the prediction tools. Results of these predictions will be compared to empirical results from wind tunnel tests. Finally, conclusions on the findings will be described, as well as suggestions for future work.

BACKGROUND

Rotor Noise Sources

The theoretical noise source mechanisms associated with rotary-wing vehicles can be divided into two categories: those of a deterministic nature and those of a nondeterministic nature. Deterministic, periodic noise sources include: thickness noise, loading noise, blade vortex interaction noise and high-speed impulsive noise.

Nondeterministic, broadband noise sources are due to turbulent flow interactions on or near the blade surface. They include turbulence ingestion noise, blade wake interaction noise and blade self-noise. Broadband self-noise will be the focus of this paper.

Self-noise is caused by the interaction between an airfoil blade and the turbulence produced in its own boundary layer and wake space (Ref. 6). If an airfoil encounters smooth inflow, self-noise is the only kind of noise generated. These self-generated noise sources are classified as follows:

Turbulent boundary layer trailing edge noise

Turbulent Boundary Layer (TBL) Trailing Edge noise is due to pressure scattering from the passage of turbulence over the trailing edge into the near-wake (Ref. 9). This occurs at higher Reynolds numbers, when turbulent boundary layers develop over most of the airfoil (Ref. 6). As the turbulence passes over the trailing edge, as seen in Figure 1(a), a mid to high frequency noise is generated as it interacts with the airfoil and its wake. This occurs on both the suction and pressure sides of the airfoil, but more prominently on the suction side for lifting rotor blades due to the increased boundary layer displacement thicknesses.

Trailing edge separation/stall noise

At higher airfoil angles of attack, boundary layer

separation begins to occur on the suction side of the airfoil, as seen in Figure 1(b), near the trailing edge. This separation can turn into deep stall noise, which would occur closer to the leading edge. Trailing edge separation/stall noise is experienced at high angles of attack due to large-scale separation in the flow, and it is a lower frequency noise similar to that of a bluff body in a flow (Ref. 6). For the remainder of this paper, this noise source will be referred to as separation noise.

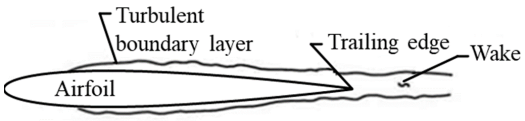

(a) TBL trailing edge noise occurring on both the pressure and suction side of an airfoil

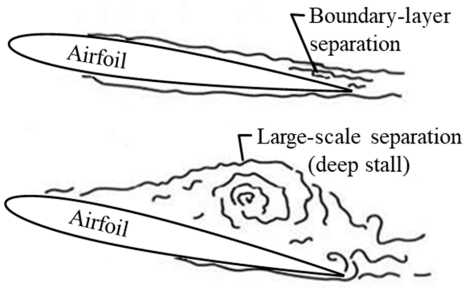

(b) Trailing edge separation/stall noise due to flow separation at high angles of attack

Fig. 1. Noise sources caused by a turbulent boundary layer (Ref. 6).

Bluntness Vortex Shedding Noise

When the airfoil geometry has a blunt trailing edge, vortices can form at the trailing edge that shed into the wake (Refs. 6,9), as seen in Figure 2. This usually occurs when the bluntness of the trailing edge is comparable to that of the boundary layer displacement thickness. This results in a high frequency noise called Bluntness Vortex Shedding (BVS) noise, which tends to dominate at high frequencies. For the remainder of this paper, this noise source will be referred to as bluntness or BVS noise.

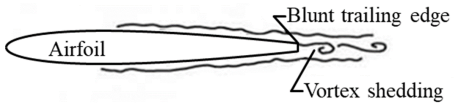

Fig. 2. Noise sources due to trailing edge bluntness vortex shedding (Ref. 6).

Tip Vortex Formation Noise

Tip vortex noise sources are a result of vortex shedding occurring at the blade tips. This source mechanism is illustrated in Figure 3. When vortices are present at the tip, they pass over the suction side and past the trailing edge of the airfoil. The interaction between the highly turbulent vortices and the airfoil and its subsequent wake generates high frequency broadband noise. When other self-noise mechanisms are present, this noise source is relatively unimportant due to its low amplitudes (Ref. 6). For this reason, the tip vortex noise source will not be discussed in the present paper.

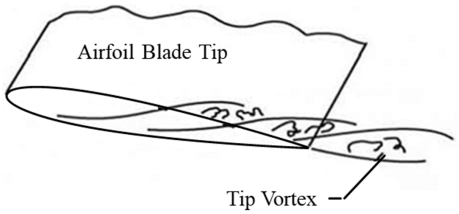

Fig. 3. Noise sources due to vortex shedding at the airfoil tip (Ref. 6).

Laminar Boundary Layer Vortex Shedding Noise

At low Reynolds numbers, a laminar boundary layer develops with instabilities that result in vortex shedding (Ref. 6). The resultant noise mechanism, laminar boundary layer vortex shedding (LBLVS), is responsible for a high frequency, "whistling" noise (Ref. 13), and is represented in Figure 4. However, LBLVS is not believed to be a significant noise source for rotors due to the unsteady flow conditions encountered by a rotating blade (Refs. 7, 10). The controlling mechanism of LBLVS noise is the presence of aeroacoustic feedback loops between the trailing edge and an upstream location on the airfoil surface where laminar instabilities occur. These feedback loops cannot form in the three-dimensional flow going over a rotor, making LBLVS noise insignificant for this study. Thus, it will not be considered in this paper.

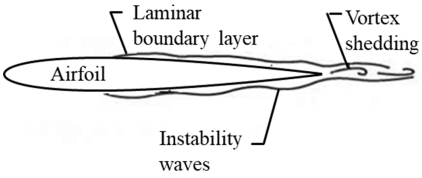

Fig. 4. Noise sources caused by laminar boundary layer vortex shedding (Ref. 6).

Hover and Forward Flight for sUAS

Fixed pitch control multicopters adjust their forward pitch, $-\alpha_v$, by varying the rotation rate between rotors. Rotors in hover ($\alpha_v = 0°$) experience considerably different inflow conditions than those in forward flight. For this and other reasons, the aerodynamics and acoustics of a quadcopter depend highly on its operating condition.

In ideal hover conditions, a rotor blade experiences azimuthally invariant velocity and angle of attack conditions as

it rotates about the hub, which results in a steady loading condition. However, lightly loaded rotors in hover are highly sensitive to disturbances in the external flow, which could affect the direction of the trailing rotor blade wakes.

In ideal forward flight, as a rotor blade rotates around its axis, it encounters a unidirectional free stream velocity V_∞, resulting in an azimuthally varying loading condition. The azimuthal variation in inflow conditions is illustrated in Figure 5. The image shows how the blade advancing toward the incoming flow experiences a higher local velocity than when it retreats away from the flow. In fact, a reverse flow region can develop, where the blade experiences high angles of attack and separation. How far inboard this region extends is directly dependent on the advance ratio $\mu = V_\infty/(\Omega R)$.

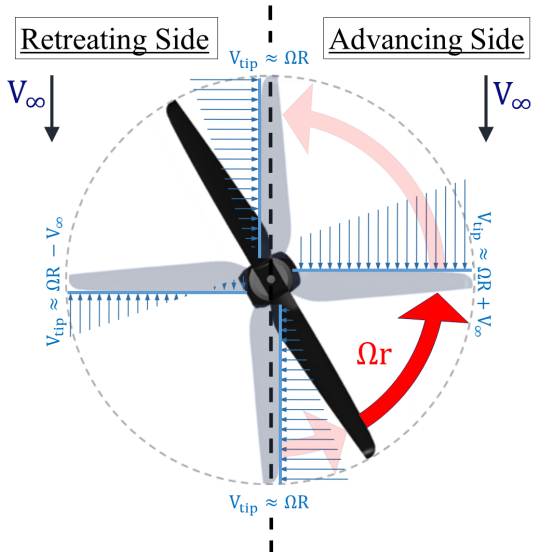

Fig. 5. Illustration of a rotor in forward flight.

EXPERIMENTAL SETUP

In 2017, a representative quadcopter model of a Straight Up Imaging (SUI) Endurance vehicle was tested in the NASA Langley Low Speed Aeroacoustic Wind Tunnel (LSAWT) to obtain acoustic and load measurements (Ref. 14). This series of experiments provided a data set for a variety of microphone array orientations, net vehicle thrust conditions and flight conditions. Isolated rotor load measurements were recently collected in LSAWT for hover and forward flight conditions. The rotor was mounted in the same configuration as the vehicle. A performance comparison between these isolated rotor LSAWT tests and the isolated rotor tests of Ref. 15 will be discussed in the Results section of this paper.

LSAWT Wind Tunnel

The LSAWT is an open-circuit free jet, acoustically treated wind tunnel currently configured for Mach number ranges of $0.045 \leq M_\infty \leq 0.140$. The facility was modified in 2017 for the purposes of small rotor testing by reconfiguring the LSAWT model test stand to mount full multicopter UAS platforms and by characterizing the facility limits for these types of tests. The LSAWT has a 28 element linear array of 6.35 mm diameter B&K model 4939 microphones, and a facility cutoff frequency of 200 Hz. For more information on the current capabilities and characteristics of the facility, see Ref. 16. The vehicle was oriented on the model test stand in LSAWT for a flyover configuration, as illustrated in Fig 6. This paper examines two flight conditions: hover and forward flight $\alpha_v = (0°, -10°)$. The freestream velocities for these flight conditions are $V_\infty = 0.0\ m/s$ & $15.5\ m/s$, respectively. This paper presents noise data from observers located underneath the vehicle ($\theta_\circ = 90°$), as well as slightly upstream ($\theta_\circ = 70°$) both at a vertical distance corresponding to +Z of -3.54 m. Observer location corrections will be discussed in a later section.

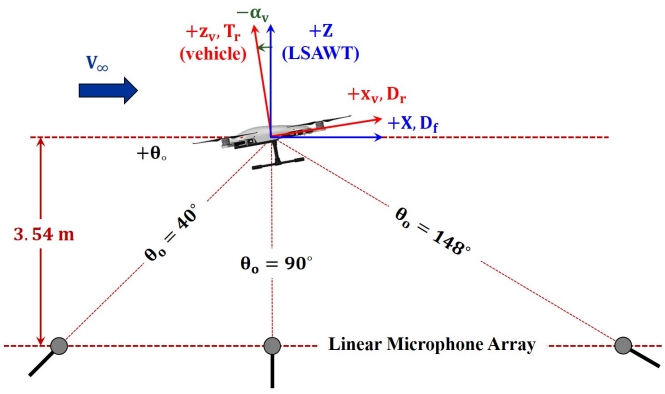

Fig. 6. Overhead microphone array location and wind tunnel properties.

SUI Endurance Vehicle Model

The full-scale vehicle model consists of an airframe, four rotors and their corresponding motors, as seen in the image in Figure 7. The rotors consist of two carbon fiber fixed-pitch blades with radii of 190.5 mm, and have a hub to hub distance of approximately 510 mm to neighboring rotors. All rotors counterrotate relative to the neighboring rotors. The tip Mach numbers in the experiment range from 0.2 to 0.3.

Load cell

A multiaxial load cell located near the center of gravity (CG) of the vehicle measured loads while the individual rotor rotation rates were trimmed to match vehicle thrust targets of 27 N, 36 N and 45 N (from here on denoted as “low”, “mid” and “high” vehicle thrust conditions). The load cell was mounted approximately in line with the landing gear support legs. The load cell is oriented in the same direction as the vehicle, with $+Z_v$ in Fig 6 corresponding to the positive thrust direction. Trim conditions were determined so that pitch, roll and yaw moments are nearly zero for the desired net thrust condition. The conditions necessary to achieve the vehicle thrust target for both hover and forward flight are presented in Table 1. Due to this vehicle having fixed-pitch control, the aft rotors

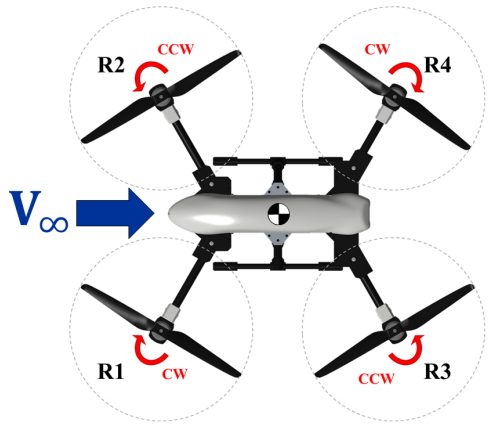

Fig. 7. CAD Model of SUI Endurance Vehicle.

spin faster by approximately 20% during a forward flight condition in order to overcome the pitching moment. The load cell setup is explained in more detail in Ref. 14.

The individual rotor thrust contributions are initially obtained from the load cell installed underneath the vehicle. However, due to the compliance of the rest of the vehicle, this load cell mounting location made it difficult to measure the thrust contribution of a single rotor. Thus, a moment arm is accounted for when processing the data. As will be discussed in the Results section, this form of load calculation had its limitations at certain conditions. For this reason, an additional set of isolated rotor tests was carried out in LSAWT recently for the two flight conditions, with the intent of gathering more accurate performance measurements. The isolated rotor was placed in the same orientations as when mounted on the vehicle. Even though the hover measurements were taken in the wind tunnel, recirculation effects on the performance were minimal when compared to previous hover chamber results (Ref. 16).

Table 1. Target vehicle thrust and rotor rotation rates for different flight conditions.

Thrust Target	Rotor Rotation Rates[a] [RPM]			
	R1	R2	R3	R4
27 N	3634/3132	3645/3158	3703/3827	3701/3827
36 N	4239/3610	4160/3641	4267/4425	4252/4412
45 N	4655/4047	4622/3992	4720/4895	4697/4937

[a]Hover/Forward Flight

Measurement Data Post-Processing

The acoustic data are processed using two techniques described in previous research (Refs. 14, 17). First, the data are treated as random data sets and the narrowband acoustic spectra are computed using the Fast Fourier Transform (FFT). Then, the periodic and random components are separated in the time domain. This is done by computing the mean rotor revolution time history and subtracting it from the time record to retain random noise components. This makes it possible to separate the nonperiodic, broadband noise from the microphone signals. For forward flight, broadband noise signals for front/aft rotor pairs are also extracted. This is accomplished by separately implementing the periodic extraction technique for each rotor, then taking the minimum of the retained random noise signals to obtain the random noise contributions for a rotor pair.

The following sound metrics are chosen to represent the data: Sound Pressure Level (SPL) spectra on both a narrowband and one-third octave basis ($SPL_{1/3}$); and integrated overall sound pressure levels unweighted (L) and A-weighted (L_A). To clearly see the trends, forward flight spectra are shown as $SPL_{1/3}$. However, due to limitations in the periodic extraction technique for hover cases, the data must be represented as narrowband SPL due to the residual tonal signals. The overall sound pressure levels are calculated over a frequency range from $200 \leq f \leq 20{,}000$ Hz, and A-Weighted (Ref. 18). For the observer microphones in the forward flight cases, Amiet's cylindrical shear layer correction (Ref. 19) is made to account for the potential refraction of sound waves present with a nonzero freestream velocity (Ref. 14). This applies an SPL amplitude correction in dB to the acoustic data, and a physical microphone location correction to calculate a corrected observer location θ_c. In addition to this, an angle offset is calculated for the position of the vehicle-installed rotors relative to the microphones. The center of gravity was located 5 inches (0.127 m) upstream of microphone 11, and each rotor was located approximately 0.25 m from the vehicle CG to which microphone 11 is originally referenced.

The hover flight condition posed several challenges when extracting the broadband signal. As explained in Ref. 14, there is a considerable amount of tonal content that extends into the higher frequency region. These harmonics had been hypothesized to be due to rotor airframe interactions (Ref. 10). Because of this, it is difficult to extract the broadband signal, as an appreciable amount of harmonics are retained. In addition to this, it is necessary to pick an observer not directly underneath the rotor, as the wake from the rotor contaminates the signal. For this paper, the observer located at $\theta_\circ \approx 70^\circ$ is chosen.

ANALYTICAL SETUP

Having processed empirical results, various modeling tools are employed to understand their limitations, as well as to categorize the noise sources present in the experiment. The prediction tools are blade element analysis techniques that predict the aerodynamic conditions and resulting noise radiation at each element. The schematic diagram in Figure 8 represents the main tool application methodology used for these predictions. Starting with the rotor blade geometry, ROTONET calculates the inflow conditions, which are input into BARC for a self-noise prediction. For some predictions, CAMRAD II is used instead of ROTONET for inflow calculations.

This paper defines the rotor and flight conditions (thrust, rotation rate, wind tunnel speed, atmospheric properties) based on the the aforementioned experiments.

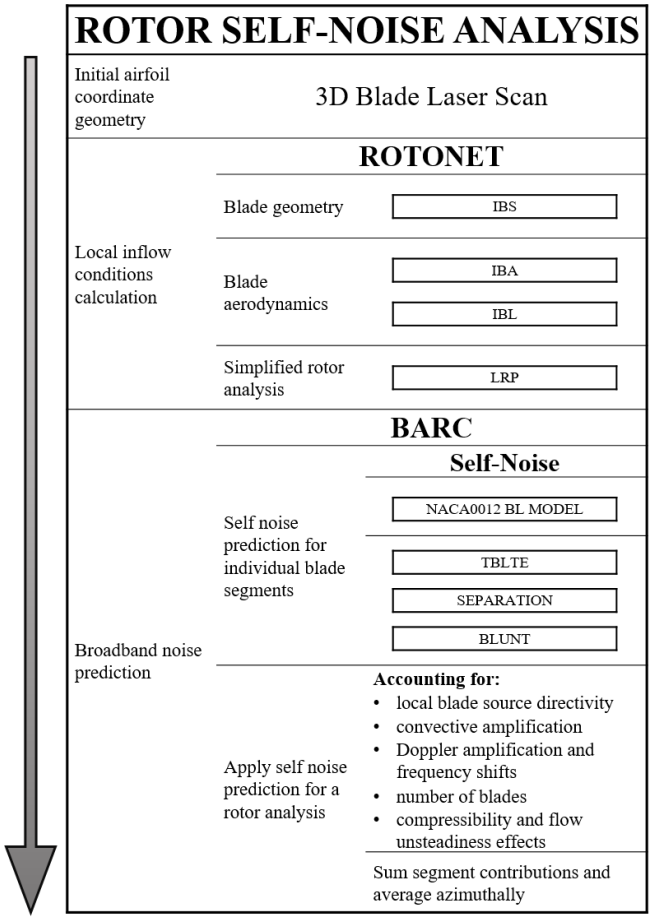

Fig. 8. Implementation of prediction tool methodology.

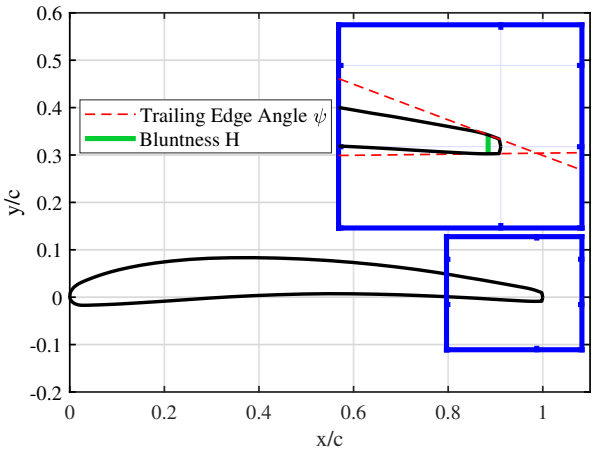

Fig. 9. SUI Endurance rotor blade airfoil at 83% span.

Blade Geometry

A three-dimensional laser scan of the T-Motor Carbon Fiber rotor blade was performed in order to generate a high resolution computational grid of the blade. Using slices from this grid, it is possible to get the airfoil geometry, which includes the twist and chord distribution for 30 radial sections. These blades have varying airfoil coordinates at each section, so the trailing edge geometry varies. There is a limit on how sharp the trailing edge can be because of manufacturing limitations at small scale. This means that the blade airfoil sections have a thickness at the trailing edge that is considerably large relative to the thicknesses of the rest of the chord, an observation that Russell comments on in Reference 20. The trailing edge bluntness thickness was measured to be 0.762 mm. Figure 9 shows coordinates for the airfoil located at a location of 83% of the span R. This corresponds to about 38% of the maximum thickness of the airfoil at that span location.

ROTONET

ROTONET is a subsystem of the NASA Aircraft Noise Prediction Program (ANOPP, Ref. 11). ROTONET uses rotor definitions and flight conditions such as thrust, rotor angle, rotor speed, advance ratio, and trim conditions as inputs in order to calculate inflow conditions for BARC. The ROTONET performance module assumes a fully articulated rotor with rigid blades and a simple uniform inflow model (Ref. 7). ROTONET is a relatively low fidelity rotorcraft analysis tool, but what it lacks in comprehensiveness it makes up for in convenience. Using the built in ANOPP modules, all that is needed for this analysis are airfoil geometries and flight conditions.

The Improved Blade Shape (IBS) module generates a numerical description of the rotor blade surface suitable for aerodynamic and acoustic calculations (Refs. 21, 22). It transforms airfoil section coordinate data from a Cartesian system to an elliptical coordinate system using an inverse Joukowski transformation. The IBS module also computes important airfoil parameters such as the zero-lift angle of attack, $\alpha_\circ$, trailing edge bluntness, H and trailing edge angle, ψ.

The Improved Blade Aerodynamics (IBA) module calculates the pressure forces acting on the upper and lower surfaces of the two-dimensional airfoil sections that make up the rotor blade (Refs. 21, 22). More specifically, the IBA module produces a table of the pressure coefficients as a function of blade coordinates, angle of attack, and Mach number.

The Improved Boundary Layer (IBL) module is used to compute the two-dimensional boundary layers on the rotor blade airfoil sections using the integral formulations for the boundary layer thicknesses. Outputs of this module include the skin friction and profile drag coefficients, as well as the trailing edge boundary layer, displacement, and momentum thicknesses for the blade airfoil sections. For reasons discussed in the Comments section, the boundary layer thickness values output by the IBL module are not used in the self-noise prediction process.

The Lifting Rotor Performance (LRP) module computes the aerodynamic force distribution on a rotor as a function of spanwise and azimuthal locations (Ref. 11). For this study, the LRP module provides the required local inflow conditions, Mach number and angle of attack, into the self-noise prediction code BARC.

CAMRAD II

The broadband noise predictions are highly dependent on the inflow conditions, boundary layer tripping condition, and load condition. For this reason, a higher fidelity tool is introduced to see if predictions could be improved. For some predictions, CAMRAD II, a comprehensive rotorcraft tool (Ref. 23), is used instead of ROTONET to calculate the local inflow conditions. CAMRAD II requires aerodynamic airfoil tables, which had been previously generated using FUN3D, for a similar SUI blade scan in Ref. 15. A pitch bearing option exists in CAMRAD II to allow the user to adjust the collective of the blade to match a certain thrust condition.

CAMRAD II contains multiple wake models, with the following two being explored in this paper: a uniform inflow model and nonuniform inflow with free wake model. Russell found that for performance, these wake models yield similar results (Ref. 20), but these models will be shown to affect the BARC self-noise prediction.

BARC

As introduced earlier, the BARC tool is a rotational frame adaptation of the self-noise method (denoted RP1218 in this paper). It calculates the self-noise contribution of each blade element at each azimuthal location and sums up the individual contributions.

In order to use the empirical boundary layer data for a prediction involving a cambered airfoil, BARC requires the zero-lift angle of attack for that airfoil as an input, which ROTONET provides. Since the SUI Endurance rotor blade has varying airfoil sections, this needs to be calculated at each radial location.

RP1218 is a self-noise prediction method with a semiempirical approach. This method models the spectral shape, level and frequency based on dependencies on Reynolds number, Mach number, airfoil geometry and boundary layer thickness (Ref. 6). The boundary layer model was developed using experimental data for a NACA 0012 airfoil. BARC relies heavily on angle of attack, and has limits on the accuracy of boundary layer curves at high angles of attack.

Comments

Some challenges associated with these prediction techniques include the following.

1. Because ROTONET was initially created for full-scale helicopter rotors, it trims a cyclic pitch and a collective pitch to match thrust for given rotation speed conditions. The SUI Endurance blades have a fixed pitch relative to the hub, and thrust is controlled by rotation speed, so these pitch adjustments may vary the effective angle of attack used in BARC from that of the experiment.
2. The LRP Module used by ROTONET assumes that the wake induced velocity normal to the hub plane is uniform over the rotor disk. This assumption needs to be taken into account when comparing predictions to experiments, as it may not represent the inflow wake present in these tests.
3. While the IBL Module is used to calculate the drag conditions at each blade element in ROTONET, BARC uses NACA 0012 data to make the broadband noise predictions. The reason for this is because IBL does not predict boundary layer thickness parameters as accurately as the empirical model described in Ref. 6 for a NACA 0012.

PERFORMANCE RESULTS

The low, mid and high thrust conditions were defined in a previous section as the individual rotational rates necessary to achieve the vehicle thrusts of 27 N, 36 N and 44 N when all rotors were running. The load cell was located at the CG of the vehicle, even for single rotor runs. Because of this, individual load values for vehicle-installed, rotor cases have to be calculated from the vehicle load measurements.

The recent isolated rotor tests had the load cell directly underneath the rotor, and thus serve as a basis for comparison. It is important to note that the LSAWT ambient conditions (speed of sound, air density, freestream velocity) were different between the vehicle-installed and isolated rotor experimental runs. More specifically, the vehicle-installed forward flight experiments were performed for a freestream condition of $M_\infty = 0.045$, while that for the isolated rotor experiments were $M_\infty = 0.048$. Therefore, the thrust comparisons between the data sets are intended to be approximate. In addition, the load values are presented in this section as dimensional thrust, rather than thrust coefficient, due to the presence of the vehicle airframe for the vehicle-installed load approximations.

Hover

In Figure 10, performance sweeps of the isolated rotor loads are compared to the SUI isolated rotor results presented in Ref. 15. The values presented by Russell were at lower RPM ranges, but both sets of data follow the same trends meaning the torque and thrust measurements are consistent with previous results at a different facility.

Individual vehicle-installed rotor loads are obtained directly from the load cell measurements. The measurements for F_Z in the $+z_v$ direction are similar to those of the isolated rotor test. This is apparent in Figure 11, where vehicle-installed individual rotor loads are compared with the isolated rotor hover performance sweep. The loads are plotted as a function of rotation rate. Included in this figure is a second-order curve fit of the isolated rotor thrust sweep. With the exception of R4, all the individual rotor loads from the vehicle tests compare reasonably well with the loads from the isolated rotor tests. The reasons for R4's lower thrust measurements are not known at this time, though it is believed to be unique to this specific set

of experimental data for this rotor in hover, and thus does not negate the previous statements.

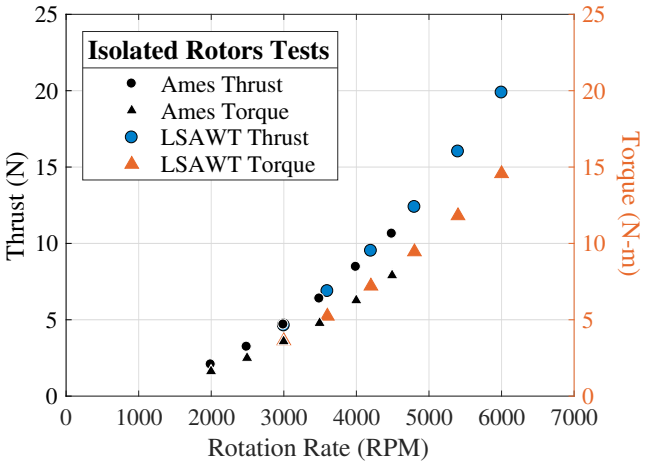

Fig. 10. Performance result comparison to previously obtained results at Ames test facility (Ref. 15).

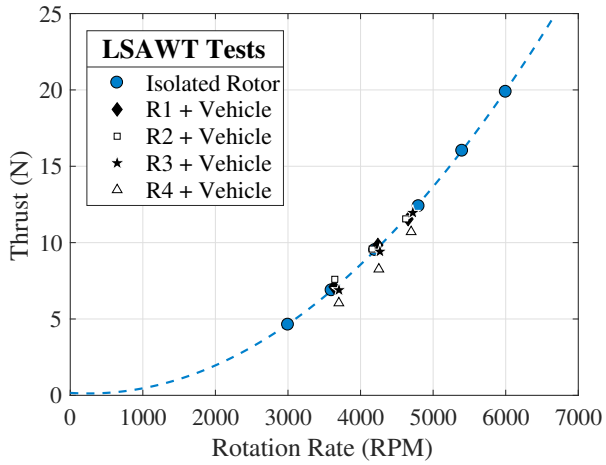

Fig. 11. Performance data comparisons between isolated rotor cases and vehicle-installed rotor cases for the hover cases (α_v = 0°, M_∞ = 0.0).

Forward Flight

Though it is relatively straightforward to extract individual rotor load measurements for the hover cases, this is difficult to do for the forward flight cases. As it is necessary to account for the moment arm mentioned earlier, load cell measurements for M_y in the $+Y$ direction are divided by the Y distance from the rotor hub to CG of L = 0.2565 m, resulting in vehicle-installed individual rotor load approximations. Figure 12 compares these approximations to the isolated rotor load data, with loads plotted against rotation rate. As with the hover case, this figure contains a second-order curve fit. The performance data of the front rotors (R1 and R2) are seen to agree reasonably well with that of the isolated rotor performance curve, while the performance data for the aft rotors (R3 and R4) are significantly lower than the isolated rotor performance curve.

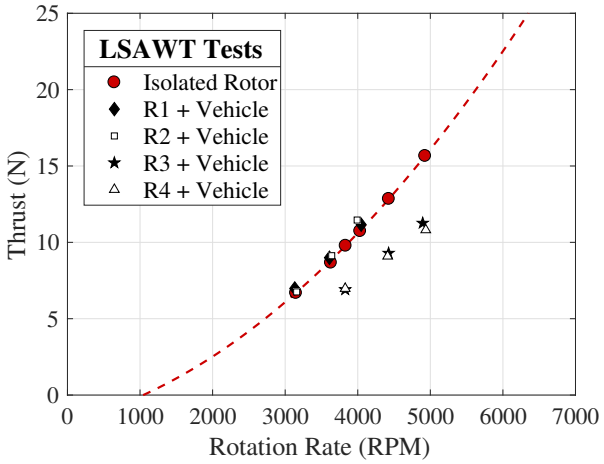

Fig. 12. Performance data comparisons between isolated rotor cases and vehicle-installed rotor cases for the forward flight cases (α_v = -10°, M_∞ = (0.045, 0.048)).

Table 2. −10° Forward flight pitch loads at the high vehicle thrust condition.

Rotor + Full Vehicle		Isolated Rotor	
Ω^a [RPM]	Thrust^b [N]	Ω^c [RPM]	Thrust^d [N]
4047/ 0 / 0 / 0	11.16	4047	10.85
0 /3992/ 0 / 0	10.81	3992	10.57
0 / 0 /4895/ 0	11.26	4895	15.47
0 / 0 / 0 /4937	11.46	4937	15.72
Total Thrust	**44.69 N**	**Total Thrust**	**52.59 N**
All Rotors in Vehicle			
Ω^a [RPM]		Full Vehicle Thrust^d [N]	
4047/3992/4895/4937		**44.34**	

[a] R1/R2/R3/R4 rotation rates,
[b] M_y/L,
[c] Isolated rotor rotation rates, calculated from the curve fit in Figure 12,
[d] F_z

Table 2 lists all the forward flight loads obtained from the vehicle tests and isolated rotor tests. The sum of the individual rotor load approximations of My/L, 44.69 N, matches the F_Z load cell measurement for the full vehicle (all rotors running) case of 44.34 N well. However, the full vehicle thrust measurement does not account for vehicle-installed rotor thrust losses. In fact, R3 & R4 produce approximately 30% less net thrust when installed in the vehicle than when they are isolated. This results in approximately 15% less vehicle thrust. This could be due to the wake of the front rotor and vehicle impinging on the inflow of the aft rotor, causing a velocity reduction. This could also be due to the download associated

with the vehicle drag ($-T_r$ in Figure 6). This vehicle download is about 2.2 N for wind tunnel flow-only conditions. For this reason, predictions in this paper will use isolated rotor performance load values to calculate inflow conditions.

Load Predictions

Initially, ROTONET is used to calculate the aerodynamic inflow conditions that BARC requires as an input. However in later predictions, CAMRAD II is used instead of ROTONET. Both tools require the thrust, rotation rates and flight conditions for each case. The loads from the isolated rotor cases are used as thrust inputs for both tools.

As highlighted before, ROTONET trims collective pitch, cyclic pitch and vehicle forward pitch to achieve the desired thrust and RPM conditions. For example, in the case of R1, the low, mid and high vehicle thrust conditions of 7, 9 and 11 N resulted in tip path angles of $\alpha_v = -14.36°$, $-10.96°$ and $-8.82°$, respectively. The collective and cyclic trim ended up being $< -3°$ for the collective and $< 1°$ for the cyclic. As a reminder, the SUI rotor has fixed pitch blades, so the cyclic trim in reality is zero. Thus, ROTONET's calculated cyclic trim is not a representation of the actual experiment.

CAMRAD II has a pitch bearing that allows the user to adjust the collective pitch index for a desired thrust condition. Because CAMRAD II performance predictions existed from Ref. 20 for the same SUI rotor blade, those predictions are rerun with updated thrust, rotational rates and flight conditions for this paper. Using the high thrust R1 case as an example, the vehicle pitch of $\alpha_v = -10°$ results in thrust calculations of $T = 8.9\,N$ and $9.3\,N$, using the uniform and free wake models, respectively. The collective trim is manually set to $-2°$ and the cyclic trim setting was off. The choice of wake model has little effects on performance calculations using CAMRAD II, as mentioned earlier.

HOVER ACOUSTICS

Figure 13 shows the implementation of the broadband extraction technique on the experimental case of an isolated rotor at the $\theta = 70°$ observer. The amplitudes of the harmonics are less for an isolated rotor than for a vehicle-installed rotor (perhaps due to airframe interaction effects). Zawodny provides discussion on the high frequency harmonic excitation that can be caused by airframe interactions in Ref. 17. Aside from this, the spectra of the vehicle-installed case are almost identical to that of the isolated rotor, so only the isolated rotor data are presented. Figure 13 shows the periodic extraction technique being used to extract out the broadband noise signal for an isolated rotor at T_r = 12.4 N, which corresponds to the high thrust condition. Yoon et al. commented on the SUI's advantages in minimal rotor-rotor interactions in hover while examining CFD for a hover case (though at lower Reynolds number and tip speeds), attributing it to the large separation distances between rotors (Ref. 4).

Though the periodic extraction technique captures several low-frequency harmonics in Figure 13, it is not able to remove

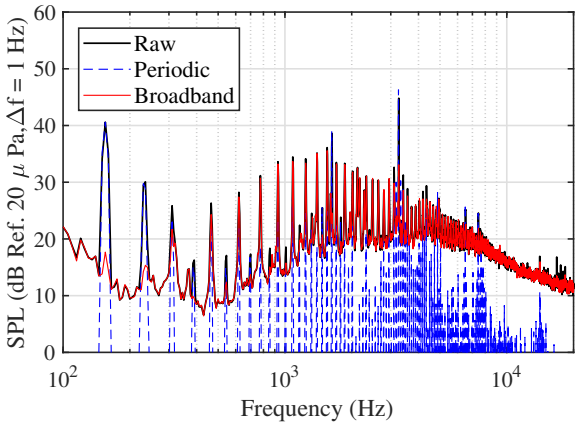

Fig. 13. Experimental data for an isolated rotor test in hover conditions ($\alpha_v = 0°$, $M_\infty = 0.0$, $\theta_\circ = 70°$).

the higher frequency harmonics. Thus, it is difficult to see the frequency transition from periodic-dominated to broadband-dominated noise. This is because recirculation effects along with tonal interactions with the airframe or the model test stand make the extraction more difficult. All this poses challenges when comparing the predictions to the experiments, but it is still possible to interpret the broadband contributions from the narrowband spectra.

Few effects on hover noise prediction are observed from the choice of inflow model. Figure 14 compares the calculated local angle of attack α as a function of blade span L/R for ROTONET's uniform inflow model, CAMRAD II's uniform inflow model, and CAMRAD II's nonuninform inflow with free wake model. The biggest difference is the inboard angle of attack being slightly higher for CAMRAD II's free wake model, which results in additional low frequency separation noise in the final prediction.

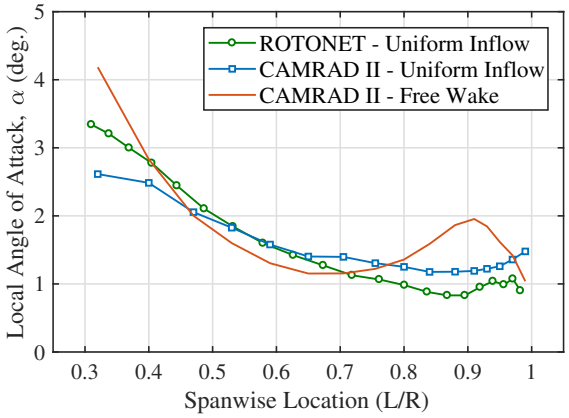

Fig. 14. Spanwise local angle of attack calculations for hover for high thrust case.

Figure 15 shows the experimental results compared to predictions using CAMRAD II calculated inflow conditions, using the free wake model. Regardless of performance tool used, the resultant BARC prediction for untripped conditions does not

capture noise in the mid frequency range. It is interesting that the tripped boundary layer condition in BARC gives remarkably better predictions than the untripped condition. A tripped prediction captures mid frequency broadband noise between 800 and 9000 Hz that the untripped prediction does not.

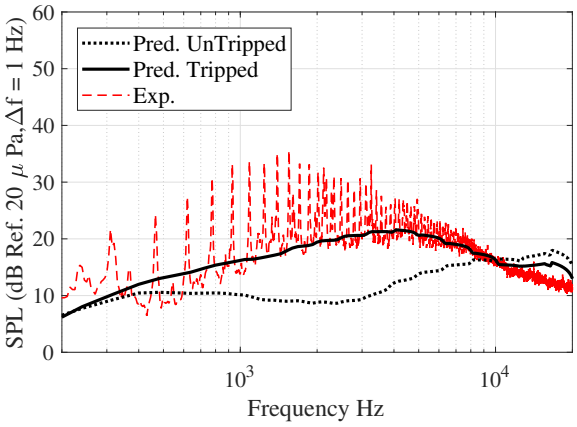

Fig. 15. CAMRAD II + BARC predictions for an isolated rotor case at (α_v = 0°, M_∞ = 0.0, $\theta_\circ$ = 70°, T_r = 12.4 N).

The breakdown of noise sources is seen in Figure 16 for both boundary layer tripping conditions. When the boundary layer is tripped, the TBLTE and separation noise peak at mid frequencies between 3000 Hz and 5000 Hz. Both these sources increase in amplitude around this range, but the separation noise increases by almost 10 dB. Bluntness noise is relatively unaffected by the tripping condition.

The tripping condition is found to give consistently better predictions for hover cases, regardless of the inflow model used. Because the SUI blades have a smooth surface, it is not expected that the tripped setting would provide a more accurate prediction.

The boundary layer thicknesses used in BARC come from the approximated curve fits of the NACA 0012 boundary layer data presented in RP1218 (Ref.6), so it seems that the boundary layer thicknesses of these hover cases are better represented by the tripped boundary layer curves. The airfoil experiments used for the boundary layer model in RP1218 were at Reynolds number conditions that ranged from 4 x 10^4 to 3 x 10^6, and angles of attack ranging from 0° to 25.2°. For reference, the local Reynolds number for the prediction in Figure 15 at 72% span is 1.7 x 10^5, and the local angle of attack is 1.14° (using ROTONET calculated inflow conditions). The RP1218 curves were created with a symmetric airfoil, which is different from the cambered, radially varying airfoils of this experiment. Though a zero-lift angle correction is applied to the effective angle of attack α calculated in CAMRAD II, it is possible that a more representative boundary layer model is needed for the cambered airfoils of these blades. An alternative reason could be effective angles of attack calculated to extract the thicknesses are not high enough. Perhaps this is an indication of the effects of an induced velocity causing

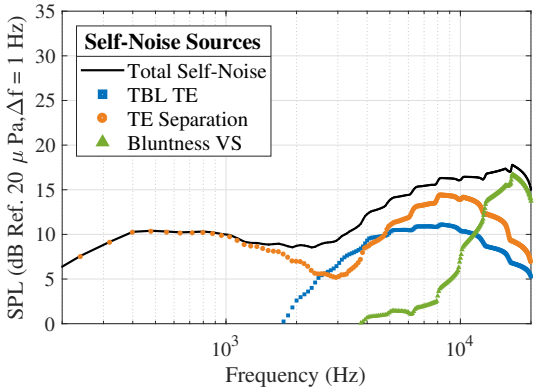

(a) Untripped boundary layer condition.

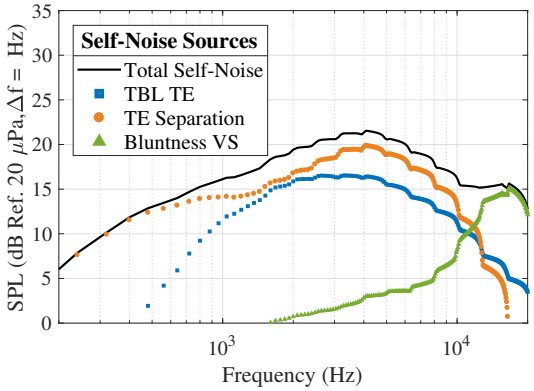

(b) Tripped boundary layer condition.

Fig. 16. Self-noise sources present in CAMRAD II + BARC predictions for R1 in hover (same conditions as Figure 15).

the angles of attack to be greater in the hover experiment, and analysis models not capturing this effect. In summary, the following observations are made for the hover acoustics data:

1. The experimental broadband extraction technique retained various harmonics for hover configurations. This means a transition to broadband dominated spectra is not as apparent. Additionally, experimental data are highly sensitive to downwash, airframe interaction, and recirculation effects at observers most affected by broadband noise from rotors in edgewise forward flight.

2. When running predictions using untripped boundary layer settings, there is a large range of unpredicted broadband noise in the 800 to 8000 Hz frequency range, regardless of performance model used. BARC only predicts self-noise sources, which are the only broadband noise sources when an airfoil encounter smooth, steady inflow. If this noise is not self-noise, then it could be due to additional broadband noise sources such as turbulence ingestion or blade wake interaction.

3. If there are no additional broadband noise sources, then the tripped boundary layer flag in BARC gives remarkably better predictions that the untripped conditions. De-

spite the airfoil being physically smooth, the boundary layer thicknesses may be higher than what is currently being predicted, either due to external flow effects from the model stand and facility, higher angles of attack experienced by the airfoils, or the application of the boundary layer model to an asymmetric airfoil.

Thus, limitations in hover self-noise predictions are attributed to underpredicted boundary layer thicknesses and/or presence of atmospheric turbulence creating a nonuniform, unsteady inflow.

FORWARD FLIGHT ACOUSTICS

After examining the aeroacoustics of the hover test data cases, the forward flight test data are examined. Reference 14 shows that the noise of the forward flight configuration has overall higher levels, mainly due to the azimuthally varying loading conditions. The front rotor R1 is analyzed first in this section. Because of its location at the front of the vehicle, the inflow it receives is relatively undisturbed. Initially, load cell measurements are obtained from the vehicle-installed cases. Unlike the hover conditions, the broadband extraction technique was more effective (see Ref. 14 for more details on this).

Front Rotor - R1

A one-third octave representation of the experimental spectra at $\theta_c = 90°$ is seen in Figure 17 for the individual R1 vehicle-installed rotor case. This figure shows the periodic signal and the corresponding residual broadband signal with little tonal content left. It is also clear to see where the noise transitions from periodic to broadband dominated noise at around 3000 Hz.

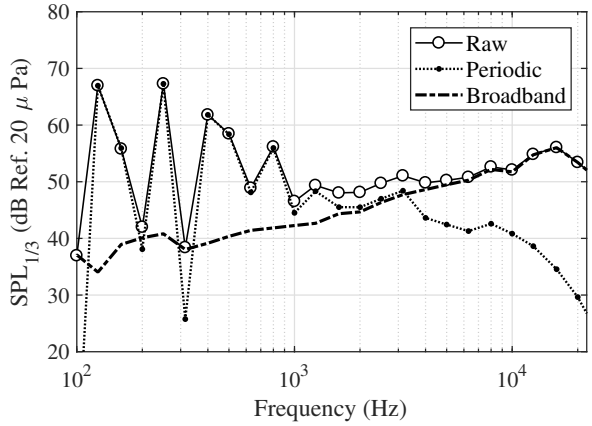

Fig. 17. Experimental noise results for R1 in forward flight, high vehicle thrust conditions ($\alpha_v = -10°$, $M_\infty = 0.045$, $\theta_c = 90°$, $T_r = 11.16$ N).

Predictions are run with the low, mid and high load conditions to see if ROTONET + BARC capture varying performance trends. The plots in Figure 18 show BARC predictions and the LSAWT experiments at the low, mid and high vehicle thrust settings. The predictions trend well with the experiments, and reasonably capture the relative changes in broadband noise with respect to frequency.

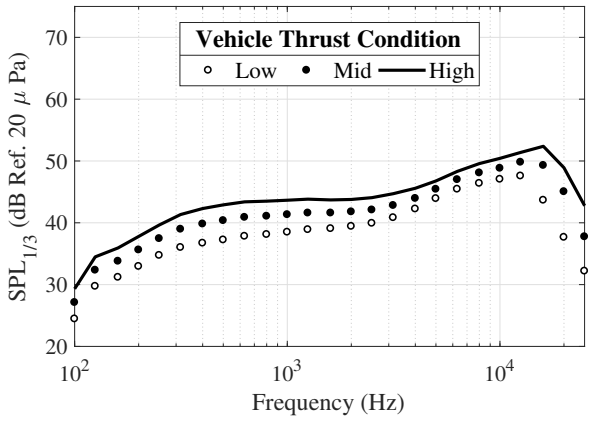

(a) ROTONET + BARC self-noise predictions.

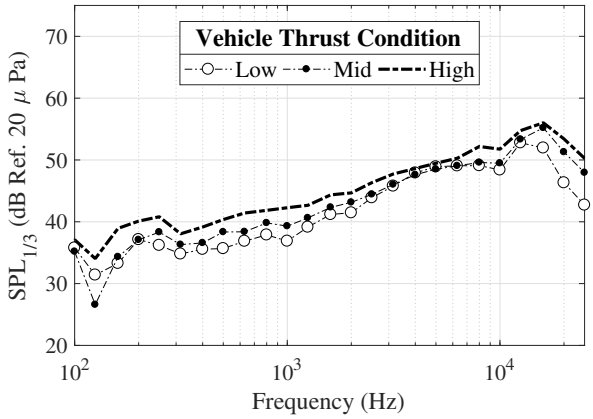

(b) LSAWT vehicle-installed tests for R1.

Fig. 18. Self-noise prediction comparison to experimental tests of R1 in forward flight for low, mid and high vehicle thrust conditions ($\alpha_v = -10°$, $M_\infty = 0.045$, $\theta_c = 90°$).

The self-noise mechanisms for the high thrust case are broken down in Figure 19. The prediction trends well with the experiment, with BARC overpredicting the noise at lower frequencies and underpredicting at frequencies above 1.6 kHz. Separation noise is the dominant noise source at low to mid frequencies. At high frequencies, above 14 kHz, bluntness noise starts to dominate. This bluntness noise is attributed to the significant bluntness of the SUI blades near the tip. TBLTE, which represents the interactions on both the suction and pressure sides, is highest at around 10 khz. The total self-noise for both the prediction and the experiment peak at 16 kHz, with a difference of about 3 dB between the two. With relatively few considerations and inputs, ROTONET + BARC are able to reasonably predict the noise at most frequencies for an observer directly underneath the vehicle, and the predictions scale well with performance conditions. Additionally, it is possible to predict noise for specific blade elements at locations r and ϕ. As mentioned in the Background section,

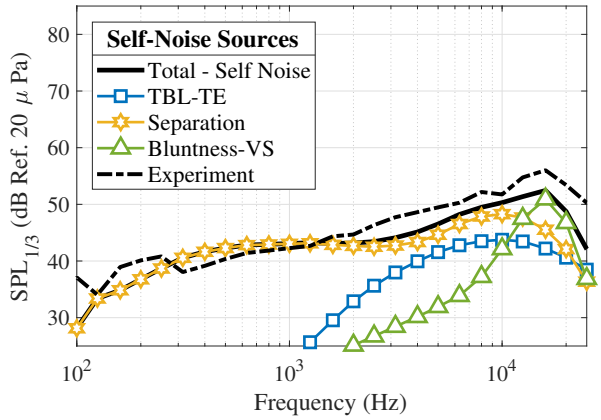

Fig. 19. ROTONET + BARC prediction for high thrust R1 for same conditions as Figure 17.

a rotor in forward flight experiences higher local velocities and angles of attack on its advancing side when modeling using uniform inflow. Because of this, most of the self-noise present on a rotor is generated on the advancing side. To verify this, BARC is run for different azimuthal and radial portions of a full rotor revolution. This is possible due to the blade element analysis nature of the code calculating the noise at each element and then summing up the results. These predictions are made with 23 radial locations and 61 azimuthal locations. ROTONET reflects the previously mentioned azimuthally varying loading in forward flight when calculating the inflow conditions, as seen in Figure 20.

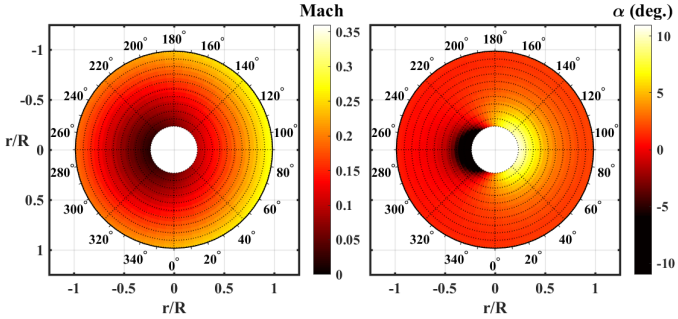

Fig. 20. ROTONET calculated inflow conditions Mach and α at each blade element for R1 in forward flight (same conditions as Figure 17).

Based upon these inflow calculations, the rotor revolution is broken up into two sections. In Figure 21(a), Section A represents the elements where the highest angles of attack are experienced, from 2.6° to 10.2°. These blade elements are located about 36% of the total radius starting at the hub, and on the advancing side between ϕ = 24° and 156°. In Figure 21(a), Section B corresponds to the outer ring starting at about 56% span to the rotor tip, which has a noticeably higher Mach number, ranging from 0.11 to 0.28. Based upon these section definitions, two separate BARC predictions are run to get Figures 21(b) and 21(c). These are then compared to the full prediction in Figure 21(d).

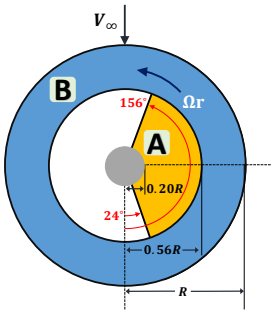

(a) Schematic of revolution sections A and B

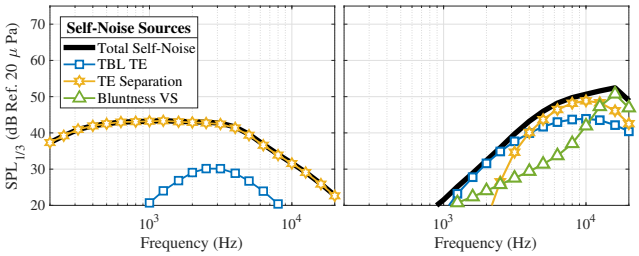

(b) Section A BARC prediction (c) Section B BARC prediction

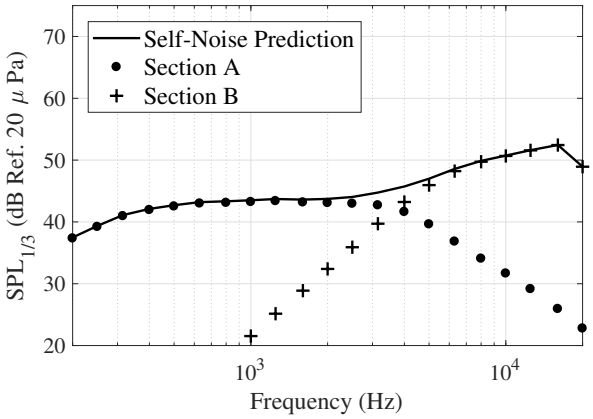

(d) Sections A + B compared with the total noise prediction

Fig. 21. BARC self-noise predictions for different revolution sections (same conditions as Figure 17).

The low frequency separation noise is the dominant noise source at the elements located on the advancing side and inner portion of the blade (section A). These predictions show that the outer radial portions of the blade experience the most bluntness vortex shedding noise, due to the significant bluntness thickness H near the tip. This outer radial location is responsible for the TBLTE noise contribution. The presence of these two sources is significant as it coincides with the 3000 Hz frequency transition point where broadband noise started dominating the rotor noise spectra. While all these noise sources are present at other azimuthal and radial locations, predictions suggest they are most dominant in these regions.

Aft Rotor - R3

Self-noise predictions for the aft rotor, R3, require additional considerations and analysis than those for R1. It is necessary to use the isolated loads instead of the installed individual rotor loads, because of the 30% thrust loss experienced while installed. All the predictions in this section are for the high vehicle thrust case.

Figure 22 shows the break down of the individual sources using ROTONET + BARC for a 15.46 N prediction, with ROTONET trimming the forward pitch to $\alpha_v \approx -7.4°$.

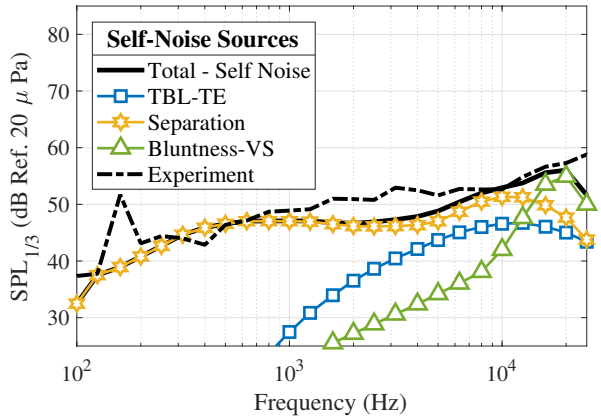

Fig. 22. ROTONET + BARC prediction for high thrust R3 at $\theta_c = 90°$.

It is apparent that BARC is underpredicting the mid frequency noise present between 1000 Hz and 7000 Hz. The approach taken to improve predictions is to use the higher fidelity tool CAMRAD II to calculate inflow conditions. This paper utilizes the following two inflow models in CAMRAD II: the uniform inflow model and the nonuniform free wake model. The most successful prediction can be seen in Figure 23, where the mid-frequency noise is more fully predicted as TBLTE and separation noise spread into the lower frequencies.

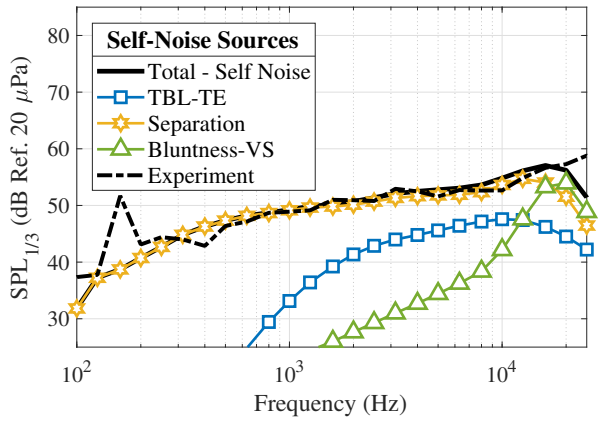

Fig. 23. CAMRAD II + BARC prediction for high thrust R3 at $\theta_c = 90°$.

Polar plots in Figure 24 show the effective angle of attack inflow condition α for ROTONET's uniform, CAMRAD II's uniform and CAMRAD II's free wake inflow. Following this, Figure 25 shows the A-Weighted and unweighted integrated overall sound pressure levels (OASPL) plot comparison for the BARC predictions using these wake models vs. the experimental data taken for the vehicle-installed, high thrust, R3 test case. These OASPL plots show that for all observer locations, both CAMRAD II's uniform inflow and free wake models result in improved BARC predictions when compared to the experiment.

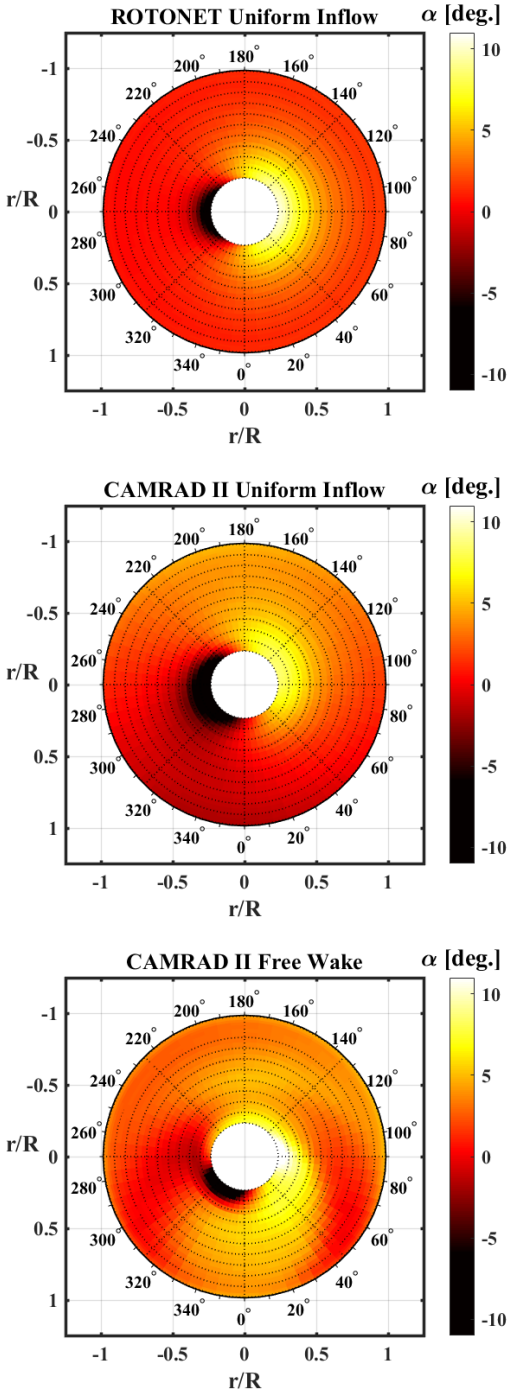

Fig. 24. Flow condition variations in forward flight for an aft rotor case.

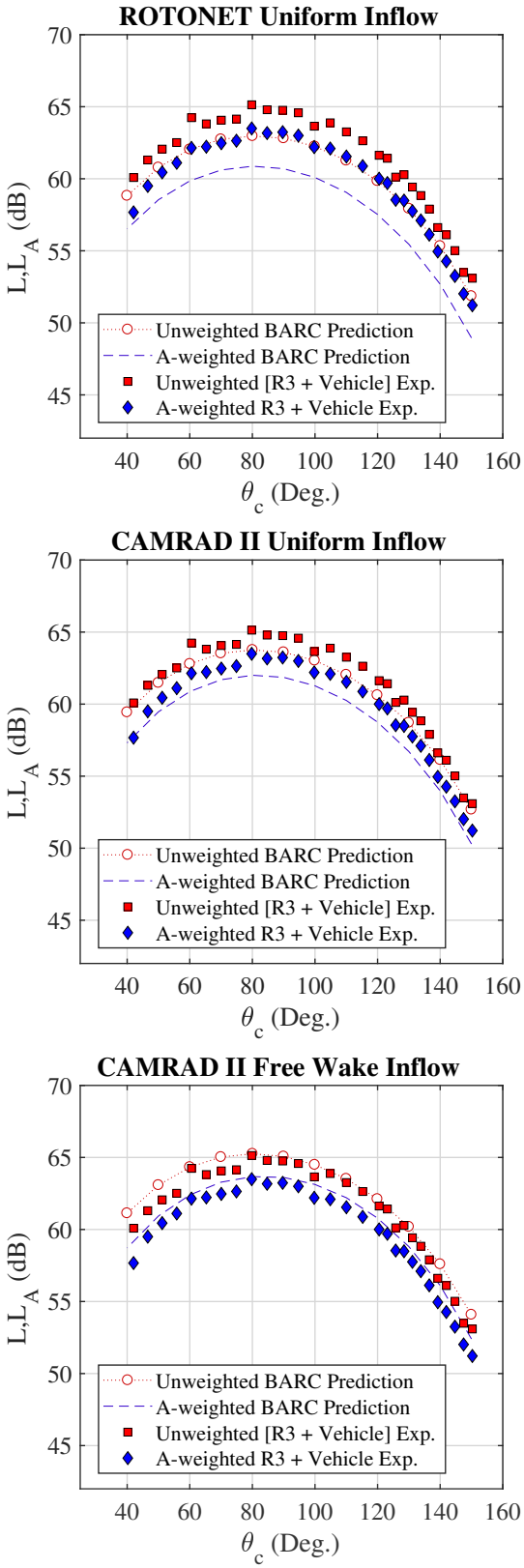

Fig. 25. Flow condition variations in forward flight for an aft rotor case.

Front and Aft Pairs

Finally, a simultaneously running front-aft rotor pair is examined, denoted as R1 & R3. The broadband extraction technique is implemented for each rotor separately, as described in the Measurement Data Post-Processing section. This is possible due to the different rotation rates at which the rotors are operating. A comparison is made with the individual rotor acoustics summed together, denoted as R1+R3, and is presented in Figure 26 for both the low and high vehicle thrust conditions.

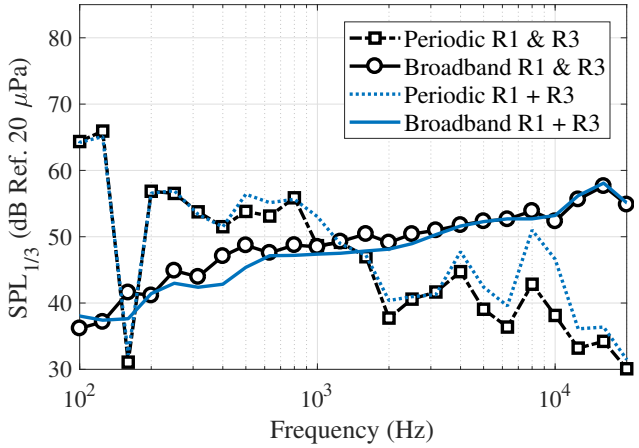

(a) Low vehicle thrust condition (T_r = 27 N).

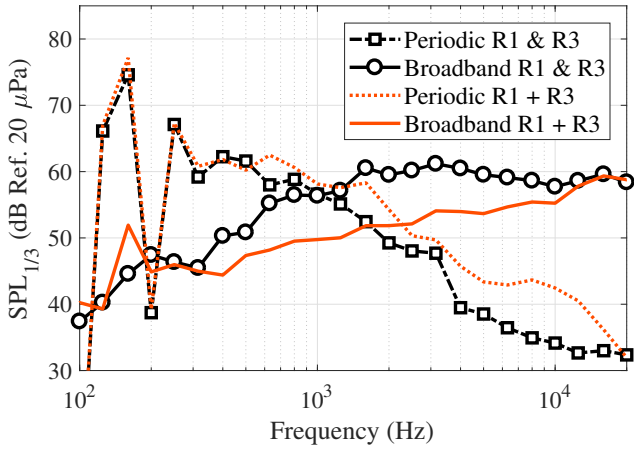

(b) High vehicle thrust condition (T_r = 45 N).

Fig. 26. Periodic and broadband contributions for superimposed individual (R1 + R3) and simultaneous (R1 & R3) LSAWT tests in forward flight ($\alpha_v = -10^\circ$, $M_\infty = 0.045$, $\theta_c = 90^\circ$).

An interesting observation for the high thrust case was made previously in Ref. 14, that additional mid frequency broadband noise is present when the two rotors are running simultaneously compared to when they are running individually, a consistent finding for all observer locations. Not only are the broadband levels higher at the mid frequencies, but the transition from periodic to broadband dominated noise occurs at an earlier frequency, despite the periodic spectrum not being

very different at these points. This is an indication of rotor turbulence ingestion or wake interaction occurring between operating rotors. However, this additional noise is not present for the low vehicle thrust condition, meaning this a thrust dependent effect.

A comparison of the summing of CAMRAD II + BARC Predictions of R1 and R3 is made with the experimental results of the high vehicle thrust case in Figure 27. The benefit of this comparison is that it highlights that the additional noise of R1 & R3 is not predicted to be due to self-noise, so attention should be given to additional broadband noise sources. Additionally, the importance of these interaction effects is that they make broadband noise dominant over a larger frequency span. It needs to be noted that while the trends match well with the superimposed R1 + R3, more research needs to be done to confirm correct inflow models are being used for these forward flight conditions.

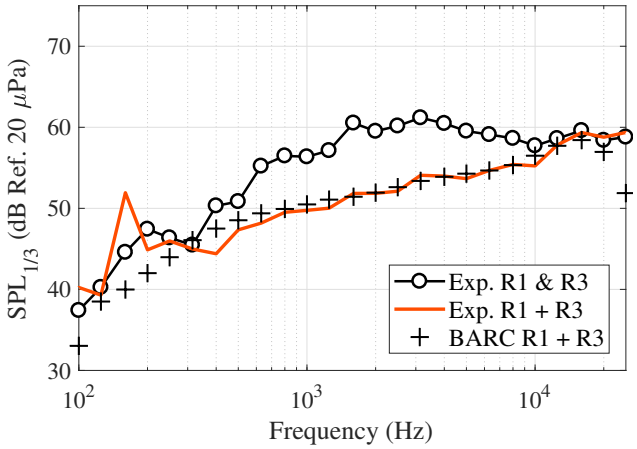

Fig. 27. CAMRAD II + BARC predictions compared to LSAWT acoustic data (same conditions as Figure 26(b)).

CONCLUDING REMARKS

This paper examines the effectiveness of a self-noise prediction methodology applied to small scale rotors, as well as an experimental broadband extraction technique. By separating out the periodic noise contributions from quadcopter experimental data, it is possible to compare the broadband noise data to self-noise predictions.

BARC is able to predict the broadband noise of the hover conditions with reasonable accuracy when a tripped boundary layer option is used. Additional steps should be taken when conducting experiments in hover, as these cases may be more sensitive to external flow effects as compared to forward flight conditions. To see if calculated boundary layer parameter are better represented by tripped conditions, additional hover prediction cases for blades with nonsymmetric airfoil blades should be made. To identify external turbulence that could cause disturbances in the inflow, a CFD solution of an isolated rotor could be computed. Additional work should be done to identify noise sources such as turbulence ingestion, additional self-noise due to a trip-like boundary layer condition, or blade wake interaction. Additional broadband noise prediction tools could be used to predict these other noise sources. Lastly, BARC should be applied to additional hover tests cases, to see if this tripped boundary layer is a more appropriate condition for small scale, rotating blades.

During forward flight high vehicle thrust conditions, there are indications of broadband noise resulting from interactions between rotors. At low thrust conditions, this additional noise was not present. Should these experiments be repeated, time should be taken to measure out the thrust underneath each rotor.

Having been previously used for larger-scale helicopter rotors, BARC has shown promise in predicting self-noise broadband noise for small rotors in forward flight and has given some understanding to the noise mechanisms and how they vary at each blade element.

This paper confirmed some of the characteristics of small scale UAS which affect noise:

1. Scale and manufacturing limitations result in blunt trailing edges, especially near the tip. This results in high frequency bluntness vortex shedding noise for forward flight conditions.

2. Rotors of this scale and shape may be highly sensitive to unsteady flow disturbances while in a hover configuration.

3. For a forward flight condition, the majority of broadband noise will generally be created on the advancing side of the blade due to trailing edge separation noise effects.

The strength of the prediction approach chosen for this paper included the flexibility in choosing which performance analysis tool is necessary for a given case. The ROTONET + BARC approach is a good starting point when a quick broadband noise prediction method is necessary as a precursor to higher fidelity predictions. This paper addressed the limitations of ROTONET by repeating predictions with CAMRAD II calculated inflow conditions. Self-noise prediction is found to be most sensitive to changes in rotor speed, thrust, and boundary layer tripping.

BARC is a valuable tool for identifying broadband noise sources caused by self-noise mechanisms. BARC is effective in identifying the noise source mechanisms, as well as trends associated with varying thrust values. It is the intention of the authors to motivate future studies with additional broadband noise prediction tools, as broadband noise is a significant noise source for small rotors in forward flight and hover operation.

Author contact

Nicole Pettingill, nicole.a.pettingill@nasa.gov

ACKNOWLEDGMENTS

The authors would like to thank Dr. Carl Russell and Dr. Douglas Boyd, for the CAMRAD II predictions and discussion they provided. Finally, they would like to give a special thanks to John Swartzbaugh, Stanley Mason, Jeffrey Collins and Bryan Lamb of the LSAWT at the Langley Research Center, for their efforts in facility test setup and data acquisition. This work was funded by the Revolutionary Vertical Lift Technology Project and the Design Environment for Novel Vertical Lift Vehicles (DELIVER).

REFERENCES

[1]Tinney, C. E. and Sirohi, J., "Multirotor Drone Noise at Static Thrust," *AIAA Journal*, Vol. 56, (7), July 2018, pp. 2816–2826.

[2]Iv, D. G., Cornelius, J., Waltermire, S., Loob, C., and Schatzman, N. L., "Acoustic Testing of Five Multicopter UAS in the U. S. Army 7- by 10-Foot Wind Tunnel," Technical Report TM-219894, 2018.

[3]Russell, C. R., Jung, J., Willink, G., and Glasner, B., "Wind Tunnel and Hover Performance Test Results for Multicopter UAS Vehicles," *AHS International 72nd Annual Forum*, 2016, pp. 3448–3467.

[4]Yoon, S., Chan, W. M., Diaz, P. V., Theodore, C. R., and Boyd Jr, D. D., "Computational Aerodynamic Modeling of Small Quadcopter Vehicles," *AHS International 73rd Annual Forum*, 2017, pp. 1–16.

[5]Amiet, R. K., "Noise due to turbulent flow past a trailing edge," *Journal of Sound and Vibration*, Vol. 47, (3), 1976, pp. 387–393.
doi: 10.1016/0022-460X(76)90948-2

[6]Brooks, T. F., Pope, D. S., and Marcolini, M. A., "Airfoil Self-Noise and Prediction," NASA RP 1218, 1989.

[7]Brooks, T. F., Marcolini, M. A., and Pope, D. S., "Main Rotor Broadband Noise Study in the DNW," *Journal of the American Helicopter Society*, Vol. 34, (2), April 1989, pp. 3–12.

[8]Burley, C. L. and Brooks, T. F., "Rotor Broadband Noise Prediction with Comparison to Model Data," 7th AIAA/CEAS Aeroacoustics Conference, Vol. AIAA/CEAS, 2001.

[9]Burley, C. L. and Brooks, T. F., "Rotor Broadband Noise Prediction with Comparison to Model Data," *Journal of the American Helicopter Society*, Vol. 49, (1), January 2004, pp. 28–42.

[10]Zawodny, N. S., Boyd Jr., D. D., and Burley, C. L., "Acoustic Characterization and Prediction of Representative, Small-Scale Rotary-Wing Unmanned Aircraft System Components," 72nd American Helicopter Society Annual Forum, West Palm Beach, FL, May 2016.

[11]Weir, S. D., Jumper, J. S., Burley, C. L., and Golub, A. R., "Aircraft Noise Prediction Program Theoretical Manual: Rotorcraft System Noise Prediction System (ROTONET), Part 4," NASA TM 83199, April 1995.

[12]Johnson, W., "A General Free Wake Geometry Calculation For Wings and Rotors," American Helicopter Society 51st Annual Forum, 1995.

[13]Roger, M. and Moreau, S., "Broadband Self Noise from Loaded Fan Blades," *AIAA Journal*, Vol. 42, (3), 2008, pp. 536–544.

[14]Zawodny, N. S. and Pettingill, N. A., "Acoustic Wind Tunnel Measurements of a Quadcopter in Hover and Forward Flight Conditions," 47th International Congress and Exposition on Noise Control Engineering, Chicago, Illinois, August 2018.

[15]Russell, C. R., Theodore, C. R., and Sekula, M. K., "Incorporating Test Data for Small UAS at the Conceptual Design Level," AHS International Technical Meeting on Aeromechanics Design for Transformative Vertical Flight: January 16 - 18, 2018.

[16]Zawodny, N. S. and Haskin, H., "Small Propeller and Rotor Testing Capabilities of the NASA Langley Low Speed Aeroacoustic Wind Tunnel," 23rd AIAA/CEAS Aeroacoustics Conference, 2017.

[17]Zawodny, N. S. and Boyd Jr., D. D., "Investigation of Rotor-Airframe Interaction Noise Associated with Small-Scale Rotary-Wing Unmanned Aircraft Systems," 73rd American Helicopter Society Annual Forum, Forth Worth, TX, May 2017.

[18]"Handbook of Aircraft Noise Metrics," Technical report, NASA CR 3406, 1981.

[19]Amiet, R. K., "Refraction of sound by a shear layer," *Journal of Sound and Vibration*, Vol. 58, (4), 1978, pp. 467–482.

[20]Russell, C. R., Field, M., and Sekula, M. K., "Comprehensive Analysis Modeling of Small-Scale UAS Rotors," AHS International 73rd Annual Forum, 2017.

[21]Nguyen, L. C., "The NASA Aircraft Noise Prediction Program Improved Propeller Analysis System," Technical report, NASA CR-4394, Hampton, VA, 1991.

[22]Zorumski, Wiliam E., Weir, D. S., "Aircraft Noise Prediction Program (ANOPP) Theoretical Manual - Propeller Aerodynamics and Noise," Technical Report TM 83199, NASA, 1986.

[23]Johnson, W., "Technology Drivers in the Development of CAMRAD II," American Helicopter Society Aeromechanics Specialists Conference, 1994.